

# High-Gain Resonant Switched-Capacitor Cell-Based DC/DC Converter for Offshore Wind Energy Systems

Amir Parastar, *Student Member, IEEE*, and Jul-Ki Seok, *Senior Member, IEEE*

**Abstract**—With the increasing integration of renewable energy generation into high-power grids, transmission at the dc level is becoming increasingly more useful than ac transmission. In this regard, emerging applications, such as offshore wind farms, require a high voltage gain dc/dc conversion system to interface with high-power transmission networks. This paper presents a new high-voltage gain resonant switched-capacitor dc/dc converter for high-power offshore wind energy systems. The proposed dc/dc converter is characterized by the resonant switching transitions to achieve minimal switching losses and maximum system efficiency. Therefore, a higher switching frequency is conceivable to attain a higher power density. The double stage output voltage of the proposed converter operates at seven times as high as the input voltage with a small device count. The output capacitors are charged and discharged continuously by a 180° phase shift with respect to each other to eliminate the output voltage ripples with the low capacitance requirements. The proposed series-modular and cascade configurations show the intrinsic advantage of being readily applicable to multistage power switching converters. The developed topology has been implemented on a 5-kW prototype converter to test its feasibility.

**Index Terms**—High-power density, high-voltage gain, offshore wind energy, resonant switched-capacitor (RSC) converter, resonant switching transitions.

## I. INTRODUCTION

OFFSHORE wind farms are growing rapidly because of their comparatively more stable wind conditions than onshore and land-based wind farms [1], [2]. Offshore 5–10-MW marine turbines are becoming more attractive for the wind power industry [3], [4]. In particular, they increase the efficiency and reduce generation cost, compared to previous wind turbine technologies [5]. The power capacities of these offshore behemoths result in an increase in the size of each component [5], [6]. Therefore, offshore wind turbine manufacturers are attempting to create an optimal design for large marine turbines. The optimized design of offshore wind turbines should cope with the

following challenges to make high-power conversion systems a feasible alternative. Bulky and huge electrical components have high investment costs because of the more difficult erection and the equipment transportation from the shore to the installation sites [7]. In addition, there is a greater need for high reliability due to the inherent lack of turbine access at sea, which makes operation and maintenance more difficult [8]. Therefore, an optimal power conversion system should feature high-power density, high efficiency, high reliability, and low costs for high-power offshore wind energy applications.

On the other hand, the longer transmission distances from offshore wind turbines to the load center lead to higher energy losses due to the low output voltage of wind turbines. In this regard, high voltage dc (HVDC) transmission promises a very flexible and efficient technology for offshore wind farms that requires power conversion systems to step-up and control the wind turbine output. A conventional HVDC system uses an ac line frequency (50/60 Hz) transformer to boost the voltage and ac/dc converters for rectification and power flow control [9]–[11]. This technology is robust and reliable, but it causes a considerable increase in weight and volume, which leads to higher installation cost. A high-power density can be obtained by replacing the bulky 50/60-Hz transformers with high-frequency transformers [12]–[14]. Unfortunately, high-frequency transformers with large turn ratios are difficult to design at high voltages and mega power levels because of the enormous expense of the magnetic material, core, and dialectic losses. One of the key-enabling components for HVDC is the high power dc/dc conversion system because it has a rigid structure, is easy to control system and more compact [15], [16].

To overcome the increasing power losses and maintain a high-power density, it is expected that large marine turbines will require a higher voltage with high-voltage gain dc/dc conversion systems to interface with the power transmission networks. Single-module dc/dc boost converters can theoretically achieve infinite voltage conversion ratios but practically, the maximum gain is limited by circuit imperfections, such as parasitic elements and switch commutation times [17], [18]. Multiple-module boost converters have been proposed to achieve high conversion ratios for applications to offshore wind farms [16]. Nevertheless, because the duty ratio of the main switch is large to achieve high-voltage gain, the switching frequency is relatively low to reduce the losses and also allows sufficient turn-off time for the switches. Therefore, increasing the size of passive elements, such as boost inductors and filter capacitors, is inevitable due to the low switching frequency.

Manuscript received November 27, 2013; revised February 7, 2014; accepted March 24, 2014. Date of publication April 1, 2014; date of current version October 7, 2014. This work was supported by the National Research Foundation of Korea (NRF) under Grant 2010-0028509 funded by the Korea government (MSIP). Recommended for publication by Associate Editor D. Vinnikov.

The authors are with the School of Electrical Engineering, Yeungnam University, Gyeongsan 712-749, Korea (e-mail: a\_parastar@ynu.ac.kr; doljk@ynu.ac.kr).

Color versions of one or more of the figures in this paper are available online at <http://ieeexplore.ieee.org>.

Digital Object Identifier 10.1109/TPEL.2014.2314110

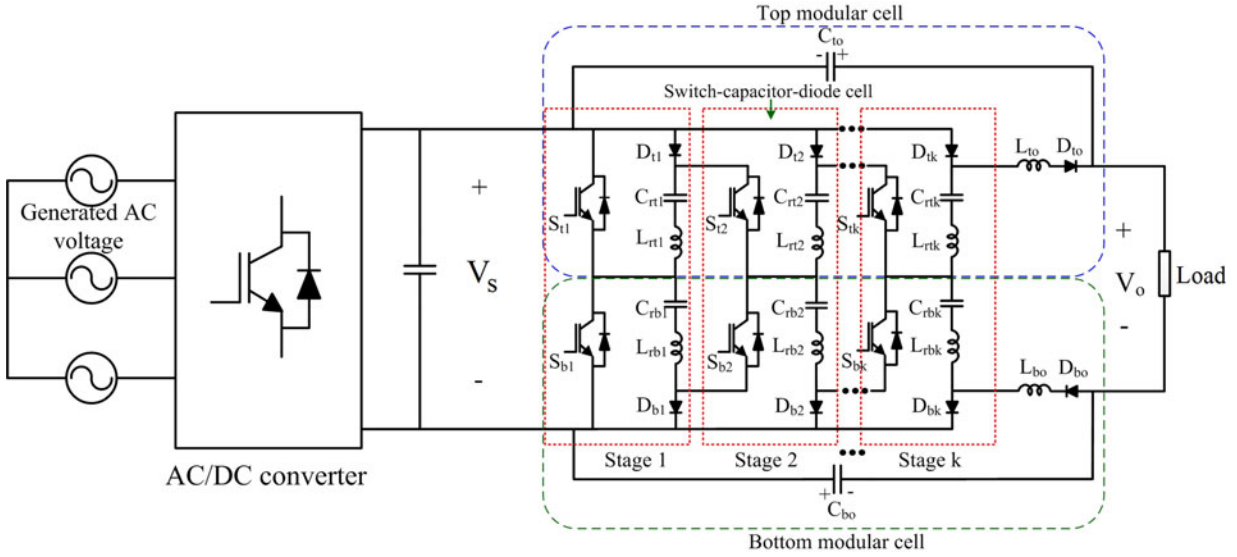


Fig. 1. Proposed RSC topology.

Recently, the common types of switched-capacitor (SC) converters are considered as an attractive solution for meeting the requirements, such as high-power density and control simplicity. In [19], a resonant SC (RSC) converter was investigated, where an extra inductor was added to form a sinusoidal manner with the capacitors to perform a soft switching. In [20], a multilevel RSC topology was proposed with significant benefits, including a modular structure, low-voltage stress of the switches, and reduced switching loss. On the other hand, the large number of capacitors, high passive component losses, and inevitably large physical size of the converters have limited the use of these topologies in high-voltage gain offshore wind energy systems. A 55-kW  $3 \times$  (the output voltage is three times the input voltage) flying-capacitor dc/dc converter was introduced for hybrid electric vehicles [21]. The major drawbacks are the nonmodular structure, complicated switching scheme, and low-voltage gain. An RSC voltage tripler with interleaving capability and high efficiency was presented in [22]. Nevertheless, it still has several problems including the passive component counts when a high-voltage gain is required for high-power applications due to the low-voltage conversion ratio of the circuit.

To solve the problems listed previously, this paper presents a new high-gain RSC dc/dc converter for offshore wind energy systems. The proposed converter combines the output of two modular cells to reduce the device count, output capacitance requirements, and total capacitor power rating. The principle of a soft-switching operation and output voltage analysis of the proposed converter are described in detail. The output capacitors are charged and discharged continuously by a  $180^\circ$  phase shift with respect to each other to eliminate the output voltage ripples without adding extra components. In this paper, the series-modular and cascade RSC configurations are introduced to increase the reliability and reduce the control complexity. These configurations are verified by a simulation and their efficiency, volume, weight, and device count are compared with a

counterpart to highlight its advantages for high voltage and high-power offshore winds applications. A comprehensive collection of the experiments are carried out to evaluate the feasibility of the proposed converter.

## II. PROPOSED RSC CONFIGURATION

### A. General Topology

Fig. 1 shows the general configuration with a three-phase generated ac voltage and an ac/dc converter in the front-end of the proposed RSC converter. A large capacitor is assumed to be used for energy storage at the output of the ac/dc converter. The RSC converter consists of two modular cells which use a new arrangement of the solid-state switches, diodes, capacitors, and inductors.

### B. Principle of the Proposed RSC Converter Operation

Fig. 2 presents a seven-level RSC converter with two stages. The RSC converter is composed of four resonant capacitors ( $C_{rt1}$ ,  $C_{rt2}$ ,  $C_{rb1}$ , and  $C_{rb2}$ ), two output filter capacitors ( $C_{to}$  and  $C_{bo}$ ), four resonant inductors ( $L_{rt1}$ ,  $L_{rt2}$ ,  $L_{rb1}$ , and  $L_{rb2}$ ), two output resonant inductors ( $L_{to}$  and  $L_{bo}$ ), six diodes ( $D_{t1}$ ,  $D_{t2}$ ,  $D_{bo}$ ,  $D_{b1}$ ,  $D_{b2}$ , and  $D_{bo}$ ), and four switches ( $S_{t1}$ ,  $S_{t2}$ ,  $S_{b1}$ , and  $S_{b2}$ ). In this paper, subscripts “t” and “b” represent the corresponding variables to the circuit components at the top and bottom cells, respectively. The switches ( $S_{t1}$ ,  $S_{t2}$ ) and ( $S_{b1}$ ,  $S_{b2}$ ) are controlled complementarily with a 50% duty cycle to minimize the conduction losses in the power devices and passive components [22]. Here, the following assumptions are made to simplify the analysis:

- 1) all the switches, diodes, capacitors, and inductors are ideal;
- 2) all the capacitances are equal and the inductors have the same values;

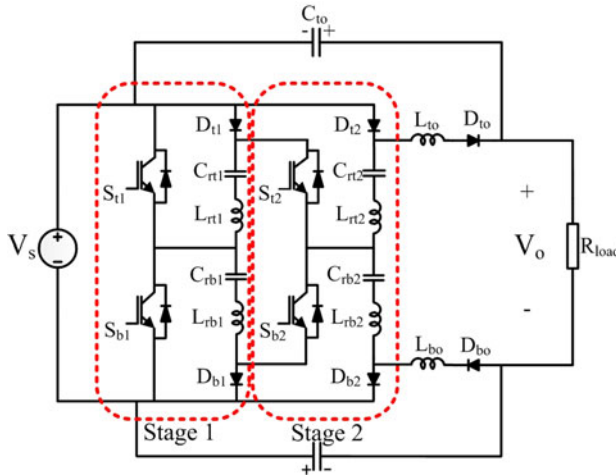


Fig. 2. Seven-level RSC converter.

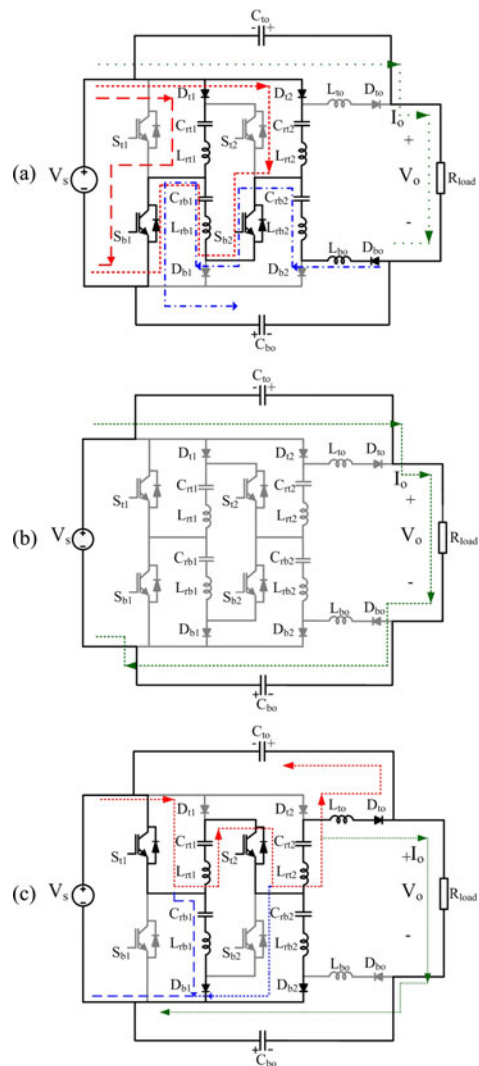
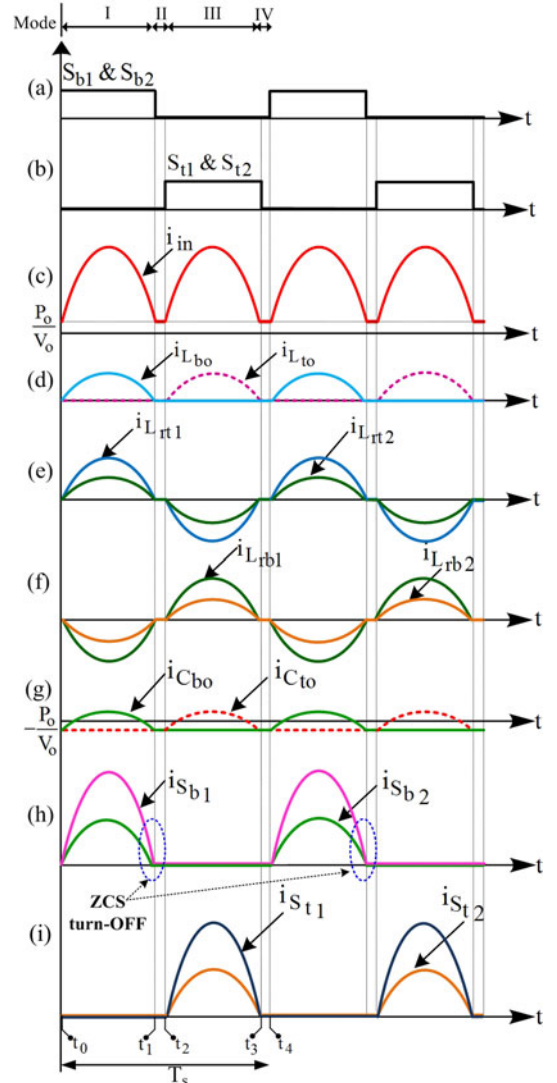
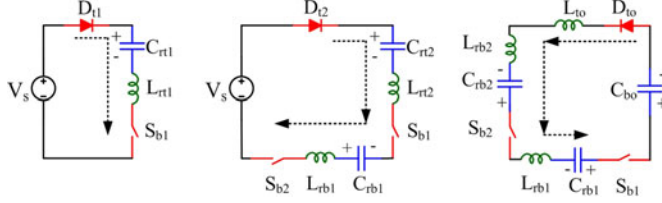
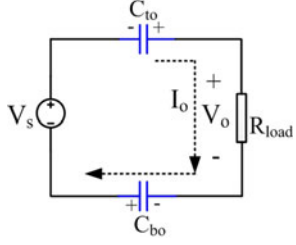
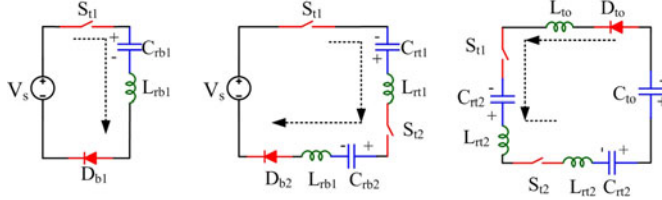
Fig. 3. Operating modes of the seven-level RSC converter. (a) Mode I  $[t_0, t_1]$ . (b) Mode II  $[t_1, t_2]$  and Mode IV  $[t_3, t_4]$ . (c) Mode III  $[t_2, t_3]$ .

Fig. 4. Key waveforms of the seven-level RSC converter at the steady-state. (a) and (b) Switching patterns. (c) Input current. (d) Output inductor currents. (e) and (f) Resonant inductor currents. (g) Output capacitor currents. (h) and (j) Switch currents.

- 3) the switching frequency is less than the resonant frequency to achieve a zero-current switching (ZCS) [17];
- 4)  $V_s$  is an ideal dc-voltage source and the load is modeled by a pure resistor ( $R_{load}$ ).

*1) Mode I* [ $t_0, t_1$ ] [see Fig. 3(a)]: In the beginning of this mode ( $t = t_0$ ),  $S_{b1}$  and  $S_{b2}$  are ON, whereas  $S_{t1}$  and  $S_{t2}$  are OFF [see Fig. 4(a) and (b)]. The diodes  $D_{b1}$  and  $D_{b2}$  are reverse biased. The charging currents flow through  $(D_{t1}, S_{b1})$  and  $(D_{t2}, S_{b2})$ , as shown in Fig. 3(a). In the top cell,  $C_{rt1}$  and  $C_{rt2}$  are charged, whereas  $C_{rb1}$  and  $C_{rb2}$  are discharged to  $C_{bo}$  in the bottom cell ( $C_{rb1}$  and  $C_{rb2}$  were previously charged at one and two times the input voltage level in Mode III, respectively) through a resonant phenomenon [see the red dotted, red dashed, and blue dotted-dashed lines in Fig. 3(a)]. Fig. 5 shows the simplified equivalent circuits in this mode. The resonant inductor currents rise and then fall in a sinusoidal manner, as shown in Fig. 4(e) and (f).  $S_{b1}$  and  $S_{b2}$  can then be OFF under the

Fig. 5. Simplified equivalent circuits of Mode I [ $t_0, t_1$ ].Fig. 6. Simplified equivalent circuit of Mode II [ $t_1, t_2$ ] and IV [ $t_3, t_4$ ].Fig. 7. Simplified equivalent circuits of Mode III [ $t_2, t_3$ ].

zero-current condition. Here, opposite energy transmission is not allowed because \$D\_{t1}\$, \$D\_{t2}\$, and \$D\_{bo}\$ make three unidirectional paths in the resonant circuit and block the reverse current flows (see Fig. 5).

2) *Mode II* [ $t_1, t_2$ ] [see Fig. 3(b)]: In this mode, all the switches and diodes are turned OFF. The resonances stop at three loops as shown in Fig. 3(b). Therefore, the inductor currents are equal to zero.

The resonant capacitor voltages of \$C\_{rt1}\$, \$C\_{rt2}\$, \$C\_{rb1}\$, and \$C\_{rb2}\$ are unchanged. The output capacitor voltages of \$C\_{to}\$ and \$C\_{bo}\$ (\$C\_{bo}\$ and \$C\_{to}\$ were charged up to three times the input voltage in Modes I and III, respectively) are discharged to the load, as shown in Fig. 6.

3) *Mode III* [ $t_2, t_3$ ] [see Fig. 3(c)]: At the instant \$t = t\_2\$, \$S\_{t1}\$ and \$S\_{t2}\$ are turned ON, while \$S\_{b1}\$ and \$S\_{b2}\$ are OFF. It can be seen from Fig. 4(j) that the currents through \$S\_{t1}\$ and \$S\_{t2}\$ are increased by a soft-switching operation with the half-cycle resonant shape. In this mode, \$C\_{rt1}\$ and \$C\_{rt2}\$ are discharged to \$C\_{to}\$, whereas \$C\_{rb1}\$ and \$C\_{rb2}\$ are charged through a resonant phenomenon as shown in Figs. 3(c) and 7. In this mode, \$D\_{b1}\$, \$D\_{b2}\$, and \$D\_{bo}\$ make three unidirectional paths in the resonant circuit to avoid opposite energy transmission. The current through \$L\_{to}\$ is decreased to zero after the half-resonant period [see Fig. 4(d)]. At the time of \$t\_3\$, \$S\_{t1}\$, and \$S\_{t2}\$ become OFF under the zero-current condition, as illustrated in Fig. 4(j).

4) *Mode IV* [ $t_3, t_4$ ] [see Fig. 3(b)]: The operation of this mode is similar to that of Mode II. Therefore, all the switches and diodes are turned OFF. The resonances stop at three loops

and the inductor currents are equal to zero [see Fig. 4(d), (e), and (f)].

Applying the charge balance principle to \$C\_{to}\$ leads to

$$-\int_{t_0}^{t_2} \frac{P_o}{V_o} dt = -\int_{t_2}^{t_3} \left( i_{L_{to}}(t) - \frac{P_o}{V_o} \right) dt + \int_{t_3}^{t_4} \frac{P_o}{V_o} dt \quad (1)$$

where \$P\_o\$ and \$V\_o\$ are the output power and output voltage, respectively. From Fig. 4, by ignoring the impact of the short times \$t\_1 \leq t \leq t\_2\$ and \$t\_3 \leq t \leq t\_4\$, it can be assumed that \$t\_0 = 0\$, \$t\_1 = t\_2 \approx T\_s/2\$, and \$t\_3 = t\_4 \approx T\_s\$, then (1) can be rewritten as

$$i_{L_{to}}(t) = -\frac{\pi P_o}{V_o} \sin(\omega_r t) \quad (2)$$

where \$T\_s\$ and \$\omega\_r\$ (\$\omega\_r = 2\pi/T\_s\$) are the switching period and the resonant frequency (\$1/\sqrt{C\_{rt1}L\_{rt1}}\$).

By applying the principle of charge balance to \$C\_{rt2}\$

$$\int_0^{T_s/2} i_{C_{rt2}}(t) dt = \int_{T_s/2}^{T_s} i_{L_{to}}(t) dt \quad (3)$$

Therefore, the resonant capacitor and inductor currents, and the output filter capacitor currents of \$C\_{to}\$ and \$C\_{bo}\$ are

$$i_{C_{rt2}}(t) = i_{L_{rt2}}(t) = \frac{\pi P_o}{V_o} \sin(\omega_r t) \quad (4)$$

$$i_{C_{rt1}}(t) = i_{L_{rt1}}(t) = \frac{2\pi P_o}{V_o} \sin(\omega_r t) \quad (5)$$

$$i_{C_{to}}(t) = \begin{cases} -\frac{P_o}{V_o} & 0 \leq t \leq T_s/2 \\ -\frac{\pi P_o}{V_o} \sin(\omega_r t) - \frac{P_o}{V_o} & T_s/2 \leq t \leq T_s \end{cases} \quad (6)$$

$$i_{C_{bo}}(t) = \begin{cases} \frac{\pi P_o}{V_o} \sin(\omega_r t) - \frac{P_o}{V_o} & 0 \leq t \leq T_s/2 \\ -\frac{P_o}{V_o} & T_s/2 \leq t \leq T_s \end{cases}. \quad (7)$$

For the k-stage of the proposed RSC converter as shown in Fig. 1, the resonant inductor or capacitor currents, input current, switch currents, diode currents, and output voltage can be expressed, respectively, as follows:

$$i_{L_{rh}}(t) = \frac{2^{k-h}\pi P_o}{V_o} \sin(\omega_r t), \quad (h = 1, 2, \dots, k) \quad (8)$$

$$i_{L_{rbh}}(t) = -\frac{2^{k-h}\pi P_o}{V_o} \sin(\omega_r t), \quad (h = 1, 2, \dots, k) \quad (9)$$

$$i_{in}(t) = \frac{P_o}{V_o} + \left| (2^k - 1) \frac{\pi P_o}{V_o} \sin(\omega_r t) \right| \quad (10)$$

$$i_{S_{th}}(t) = \begin{cases} 0 & 0 \leq t \leq T_s/2 \\ -\frac{2^{k-h+1}\pi P_o}{V_o} \sin(\omega_r t) & T_s/2 \leq t \leq T_s \end{cases}, \quad (h = 1, 2, \dots, k) \quad (11)$$

$$i_{S_{bh}}(t) = \begin{cases} \frac{2^{k-h+1}\pi P_o}{V_o} \sin(\omega_r t) & 0 \leq t \leq T_s/2 \\ 0 & T_s/2 \leq t \leq T_s \end{cases}, \quad (h = 1, 2, \dots, k) \quad (12)$$

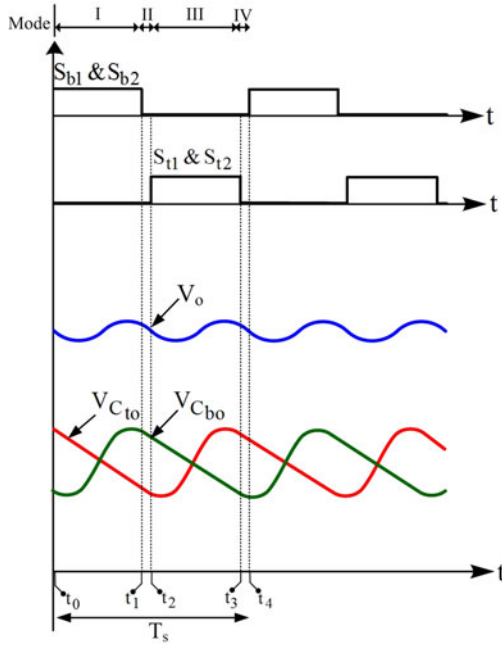


Fig. 8. Key steady-state voltage waveforms of the output and filter capacitors.

$$i_{D_{th}}(t) = \begin{cases} \frac{2^{k-h}\pi P_o}{V_o} \sin(\omega_r t) & 0 \leq t \leq T_s/2 \\ 0 & T_s/2 \leq t \leq T_s \end{cases}, \quad (13)$$

(h = 1, 2, ..., k)

$$i_{D_{bh}}(t) = \begin{cases} 0 & 0 \leq t \leq T_s/2 \\ -\frac{2^{k-h}\pi P_o}{V_o} \sin(\omega_r t) & T_s/2 \leq t \leq T_s \end{cases}, \quad (14)$$

(h = 1, 2, ..., k)

$$V_o = (2^{k+1} - 1)V_s. \quad (15)$$

A detailed derivation of the mathematical equations for the proposed  $k$ -stage converter is presented in the Appendix. It can be observed from (15) that the proposed  $k$ -stage RSC converter inherently offers the potential for the large gains by the lowest number of passive components and switches due to the exponential effect.

### C. Output Voltage Analysis of the Proposed RSC Converter

As explained in Section II-B, when  $C_{to}$  is discharged to the load in the top cell,  $C_{bo}$  is charged through  $C_{rb1}$  and  $C_{rb2}$  in Mode I [see Fig. 4(g)]. Therefore, the top and bottom cells operate  $180^\circ$  out of phase. Fig. 8 shows key steady-state voltage waveforms of the output and filter capacitors for the seven-level RSC converter. The voltage of  $C_{to}$  during the discharging process can be analyzed from the  $RC$  circuit with the load and during the charging state can be expressed in a sinusoidal form from (6).

If the initial voltage of  $C_{to}$  at  $t_0 = 0$  is assumed to be  $V_{Ct0}$ , then the capacitor voltage function of  $C_{to}$  can be expressed as

$$V_{C_{to}} = \begin{cases} V_{Ct0} e^{-t/\tau_{RC}} & 0 \leq t \leq T_s/2 \\ V_{Ct0} e^{-\pi/\tau_{RC}} + \frac{\pi P_o}{C_{to}\omega_r V_o} (\cos(\omega_r t) + 1) - \frac{P_o(t - \pi)}{C_{to}\omega_r V_o} & T_s/2 \leq t \leq T_s \end{cases} \quad (16)$$

where  $\tau_{RC}$  ( $\tau_{RC} = R_{load}C_{to}$ ) is the time constant of the  $RC$  circuit. It can be noted that both output capacitors  $C_{to}$  and  $C_{bo}$  are discharged to the load with the  $\tau_{RC} = R_{load} \left( \frac{C_{to}C_{bo}}{C_{to} + C_{bo}} \right)$  for  $t_1 \leq t \leq t_2$  and  $t_3 \leq t \leq t_4$  (see Fig. 6). However, the short times can be neglected in this analysis. Because  $\tau_{RC}$  is much larger than  $T_s$ , the discharge from  $C_{to}$  to the load can be approximated linearly and the output filter capacitor voltages are obtained as follows:

$$V_{C_{to}} = \begin{cases} V_{Ct0} - \frac{P_o t}{C_{to}\omega_r V_o} & 0 \leq t \leq T_s/2 \\ V_{Ct0} + \frac{\pi P_o}{C_{to}\omega_r V_o} + \frac{\pi P_o}{C_{to}\omega_r V_o} \cos(\omega_r t) - \frac{P_o t}{C_{to}\omega_r V_o} & T_s/2 \leq t \leq T_s \end{cases} \quad (17)$$

$$V_{C_{bo}} = \begin{cases} V_{Cb0} - \frac{\pi P_o}{C_{bo}\omega_r V_o} \cos(\omega_r t) + \frac{\pi P_o}{C_{bo}\omega_r V_o} - \frac{P_o t}{C_{bo}\omega_r V_o} & 0 \leq t \leq T_s/2 \\ V_{Cb0} + \frac{2\pi P_o}{C_{bo}\omega_r V_o} - \frac{P_o t}{C_{bo}\omega_r V_o} & T_s/2 \leq t \leq T_s \end{cases}. \quad (18)$$

The output voltage is the sum of the output filter capacitor voltages and input voltage. The resulting voltage has a frequency that is two times that of the switching frequency. The inherent interleaving property of the proposed circuit effectively reduces the output voltage ripple value without adding extra components. Therefore, the output capacitance requirement is one third of the capacitance in the conventional RSC converters for the same output voltage ripple. Moreover, the voltage rating of  $C_{to}$  and  $C_{bo}$  are always  $\frac{V_o - V_s}{2}$  for the proposed circuit, whereas, in most SC and RSC converters, the output capacitor has the voltage rating value of  $V_o$  [23]–[25].

### D. Component Stress Analysis and Comparison

Based on aforementioned analysis of the proposed RSC converter in Sections II-B and C, all the components in the top cell have identical voltage and current ratings with the counterparts in the bottom cell.  $C_{rt1}$  and  $C_{rt2}$  need to sustain voltages of  $V_s$  and  $2V_s$ , respectively. Therefore, the voltage stresses of  $S_{t1}$  and  $S_{t2}$  are the same as the capacitor voltages of  $C_{rt1}$  and  $C_{rt2}$  [see Fig. 3 (a) and (c)]. From (6), the rms currents of  $C_{to}$  and  $C_{bo}$

TABLE I  
VOLTAGE AND CURRENT RATINGS OF THE COMPONENTS FOR THE PROPOSED AND ZCS-RSC CONVERTERS

Topology	Proposed converter	ZCS-RSC converter[20]
No. of resonant capacitors	4	6
No. of resonant inductors	6	6
No of output filter capacitors	2	6
Voltage rating of resonant capacitors	$V_s$ and $2V_s$	$V_s$
Current rating of resonant capacitors and inductors	$2\pi I_o, \pi I_o$	$3\pi I_o, 2\pi I_o, \pi I_o$
Voltage rating of filter capacitors	$3V_s$	$V_s$
Current rating of filter capacitors (RMS current)	$1.21I_o$	$4.81I_o, 2.7I_o,$ and $1.21I_o$
No. of switches	4	2
Voltage rating of switches	$V_s$ and $2V_s$	$V_s$
Current rating of switches	$4\pi I_o, 2\pi I_o$	$6\pi I_o$
No. of diodes	6	12
Voltage rating of diodes	$V_s, 3V_s$	$V_s$
Current rating of diodes	$2\pi I_o, \pi I_o$	$\pi I_o$

can be obtained as follows:

$$I_{rms-C_{to}} = \sqrt{\frac{1}{T_s} \left[ \int_0^{T_s/2} \left( -\frac{P_o}{V_o} \right)^2 dt + \int_{T_s/2}^{T_s} \left( -\frac{\pi P_o}{V_o} \sin(\omega_r t) - \frac{P_o}{V_o} \right)^2 dt \right]} = \frac{\sqrt{\pi^2 - 4}}{2} \frac{P_o}{V_o} = 1.211I_o \quad (19)$$

$$I_{rms-C_{bo}} = \sqrt{\frac{1}{T_s} \left[ \int_0^{T_s/2} \left( \frac{\pi P_o}{V_o} \sin(\omega_r t) - \frac{P_o}{V_o} \right)^2 dt + \int_{T_s/2}^{T_s} \left( -\frac{P_o}{V_o} \right)^2 dt \right]} = \frac{\sqrt{\pi^2 - 4}}{2} \frac{P_o}{V_o} = 1.211I_o. \quad (20)$$

Table I lists the voltage and current ratings of the components for the proposed converter and ZCS-RSC converter in [20] for a voltage gain of 7. The current ratings of the component are the peak values except for the output filter capacitors. It can be seen from Table I that the components have the different voltage and current ratings at the different stages. The number of resonant capacitors and output filter capacitors are smaller in the proposed circuit than in the ZCS-RSC converter. The volt-ampere rating (VAR) of a resonant capacitor is defined as the product of the average voltage rating of the resonant capacitor and average charging/discharging current flowing through it. The total VAR (TVAR) requirement of the resonant capacitors for a voltage gain of 7 can be obtained from Table I. The normalized TVARs are 8 and 12 for the proposed RSC and ZCS-RSC circuits, respectively (see Fig. 9).

The general  $TVAR_{C_r}$  equation for the proposed k-stage converter can be expressed as

$$TVAR_{C_r} = V_s I_o k 2^k. \quad (21)$$

Detailed proof of (21) is given in the Appendix.

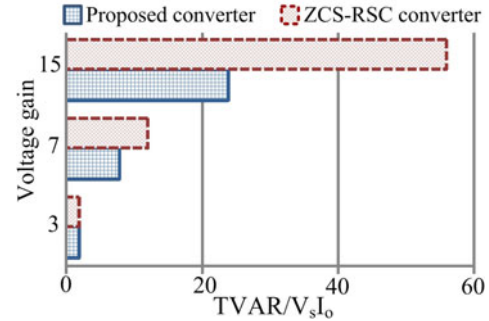


Fig. 9. Normalized TVARs of the resonant capacitors versus voltage gain.

TABLE II  
VOLTAGE AND CURRENT RATINGS OF BASE COMPONENTS

Base component	Voltage	Current
Base capacitor (C)	$V_s$	$I_o$
Base inductor (L)	-	$\pi I_o$
Base switch	$V_s$	$\pi I_o$
Base diode	$V_s$	$\pi I_o$

A base comparison is considered due to the different voltage and current stresses of the components. Table II lists the voltage and current ratings of the base components. Here, for the ZCS-RSC converter, the filter capacitors are considered to be five times larger than the resonant capacitors to achieve nearly same resonant frequency in all the resonant loops. Therefore, a filter capacitor requires five resonant capacitors in a parallel connection to gain the required capacitance. The total number of switches and diodes can be obtained with parallel and serial connections of the base switch and base diode, respectively. For example, to realize the switch with a voltage rating of  $V_s$  and a current rating of  $6\pi I_o$ , six base switches are needed in parallel to verify the current rating of the switch in the ZCS-RSC circuits (see rows 10 and 11 in Table I). Fig. 10(a) shows the total number of components for both topologies. The proposed circuit employs far fewer capacitors than those of the ZCS-RSC circuit. That is because the output capacitors have larger capacitance and higher current ratings in the ZCS-RSC circuit.

On the other hand, the total number of diodes for the proposed circuit is larger than that of the ZCS-RSC converter because of the higher voltage and current ratings of the diodes. Both converters have the same switch numbers because the proposed circuit has a lower current and higher voltage ratings of the switches, whereas the ZCS-RSC converter requires switches with the input voltage and current ratings. Finally, comparative analysis reveals that the ZCS-RSC circuit requires more passive component, which results in an larger overall size and converter cost, particularly in the higher voltage gains [see Fig. 10(b)]. High-power-density power conversion systems offer the opportunity to install lightweight components such as tower and platform systems for offshore wind energy systems.

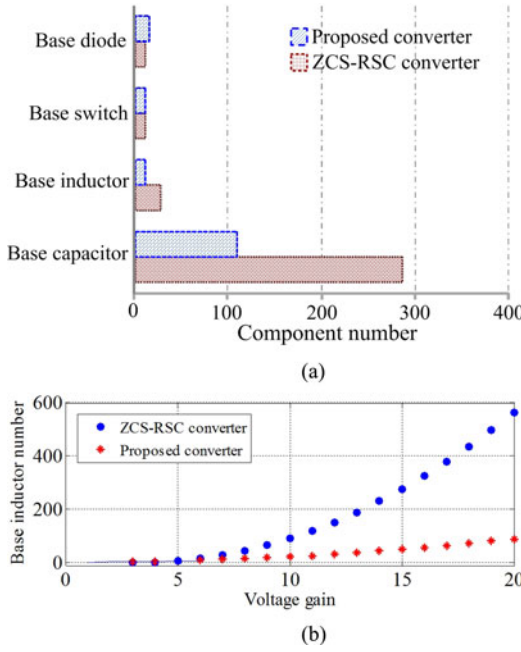


Fig. 10. Component count comparisons. (a) Component number for a voltage gain of 7. (b) Base inductor number versus voltage gain.

#### E. Power Loss Analysis

**Conduction loss of power devices:** Power device conduction loss can be calculated using a device approximation with a series connection of a dc-voltage source ( $U_o$ ), representing device on-state zero-current voltage and on-state resistance ( $R_c$ ) [26]. The average and rms currents of the power devices can be obtained from (11) and (12), as follows:

$$I_{dc-S_{th}} = I_{dc-S_{bh}} = \frac{2^{k-h+1} P_o}{V_o}, \quad (h = 1, 2, \dots, k) \quad (22)$$

$$I_{rms-S_{th}} = I_{rms-S_{bh}} = \frac{2^{k-h} \pi P_o}{V_o}, \quad (h = 1, 2, \dots, k). \quad (23)$$

Therefore, the conduction loss equations of the power devices can be derived as

$$P_{c-S_{th}} = U_{o-S_{th}} \frac{2^{k-h+1} P_o}{V_o} + R_{c-S_{th}} \left( \frac{2^{k-h} \pi P_o}{V_o} \right)^2, \quad (h = 1, 2, \dots, k) \quad (24)$$

$$P_{c-D_{th}} = U_{o-D_{th}} \frac{2^{k-h} P_o}{V_o} + R_{c-D_{th}} \left( \frac{2^{k-h-1} \pi P_o}{V_o} \right)^2, \quad (h = 1, 2, \dots, k) \quad (25)$$

$$P_{c-D_{to}} = U_{o-D_{to}} \frac{P_o}{V_o} + R_{c-D_{to}} \left( \frac{\pi P_o}{2V_o} \right)^2 \quad (26)$$

**Resonant capacitor and inductor losses:** Assume that the resonant capacitor ESR is  $R_{ESR}$ , and the resonant inductor resistance is  $R_{ESL}$ , the resonant capacitor and inductor losses can be obtained as follows:

$$P_{C_{rth}} = R_{ESR-C_{rth}} \left( \frac{2^{k-h} \pi P_o}{\sqrt{2} V_o} \right)^2, \quad (h = 1, 2, \dots, k) \quad (27)$$

$$P_{L_{rth}} = R_{ESL-L_{rth}} \left( \frac{2^{k-h} \pi P_o}{\sqrt{2} V_o} \right)^2, \quad (h = 1, 2, \dots, k). \quad (28)$$

**Output inductor and capacitor losses:** Assume that the output capacitor ESR is  $R_{ESR}$ , and the output inductor resistance is  $R_{ESL}$ , the output capacitor and inductor losses can be expressed as

$$P_{C_{to}} = R_{ESR-C_{to}} I_{rms-C_{to}}^2 = R_{ESR-C_{to}} \left( \frac{\sqrt{\pi^2 - 4} P_o}{2} \frac{V_o}{V_o} \right)^2 \quad (29)$$

$$P_{L_{to}} = R_{ESL-L_{to}} I_{rms-L_{to}}^2 = R_{ESL-L_{to}} \left( \frac{\pi P_o}{2V_o} \right)^2 \quad (30)$$

### III. SIMULATION RESULTS AND EVALUATION OF THE PROPOSED RSC CONVERTER

Offshore wind farms in the MW range are needed to interface the high voltage power networks. To cope with this situation, the proposed series-modular and cascade RSC configurations can be introduced to achieve a high-voltage gain and high rated power. A 10-MW wind turbine with an output of 6.6 kV<sub>LL,rms</sub> is considered as an input source. This voltage will be boosted to 140 kV for HVDC transmission through a three-phase ac/dc converter and the proposed series-modular RSC converter. The RSC converter by itself has a poor regulation property; it only realizes a designed high-voltage gain and high efficiency with a fixed 50% duty cycle. The ac/dc interface converter supplies a regulated input dc voltage for the RSC converter against the generated voltage variation, as shown in Fig. 1. However, this is not suitable method to regulate input dc voltage of the RSC converter under a wide range of the load variation. In order to regulate the output voltage against the load variation, a low power buck-boost converter can be connected in series with the proposed RSC converter [27]. The 14-level RSC converter was developed using MATLAB/Simulink with the PLECS Blockset [28]. The resonant frequency is set to 3 kHz. All the capacitors and inductors selected are 100  $\mu$ F and 28  $\mu$ H, respectively.

The series-modular power conversion system has an advantage regarding the reliability for offshore wind energy systems, where maintenance and exchange of parts are the main issue. For example, if a single module fails, the converter can still function, albeit at a reduced power level. The semiconductor devices in series converter experience only half the total voltage stress, which is an advantage in high voltage converters, where several switches must be connected in series to withstand the rated voltage. Two modular cells are designed for equal voltage gains of 7 and identical input powers of 5 MW. Fig. 11(a) shows the proposed series-modular configuration. Each cell A or B includes two top and bottom modular cells, as shown in Fig. 11(b) and (c). Both cells operate from equal input voltages and draw the same input currents. Fig. 12 shows the simulation waveforms for the switching patterns, input current, input currents of cells A and B, and switch currents of cell A. From Fig. 12(a) and (b), with a 90° phase shift between cells A and B, the input current ripple can be reduced significantly to the

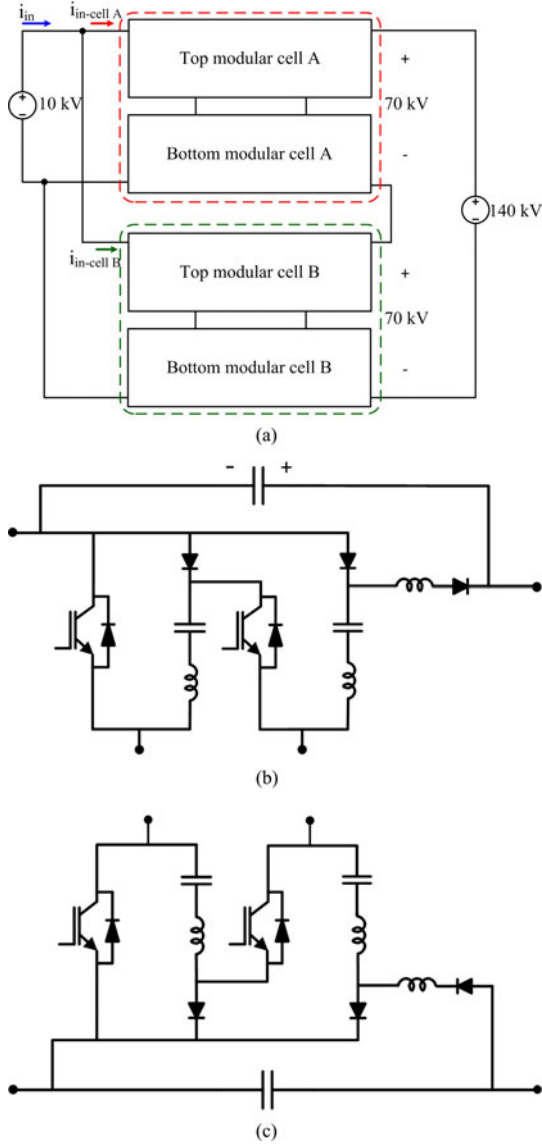


Fig. 11. (a) Proposed series-modular RSC configuration. (b) Top modular cell. (c) Bottom modular cell.

proper value of 200 A [see Fig. 12(c)]. Therefore, the input filter size can be lowered considerably by the interleaving operation. If the converter works without interleaving functionality and the two cells, A and B, operate with no phase shift, the input current ripple of the converter is twice the input current of cell A. In Fig. 12(d), the input current of each cell has a frequency two times the switching frequency, whereas the input current of the series-modular RSC converter has four times the switching frequency due to the interleaving functionality. Fig. 12(e) shows that all the switches can be ON and OFF under the zero-current condition. The simulation results closely match the analysis and operation of the proposed RSC converter in Section II. Fig. 13 shows the waveforms of the output filter capacitor voltages for the cells A and B, output voltage of cell A, output voltage, and resonant capacitor voltages of cell A. Because the output filter capacitor voltages in cell A or B have a 180° phase shift with respect to each other, the output voltage of cell A or B has a frequency two times the switching frequency. From the simu-

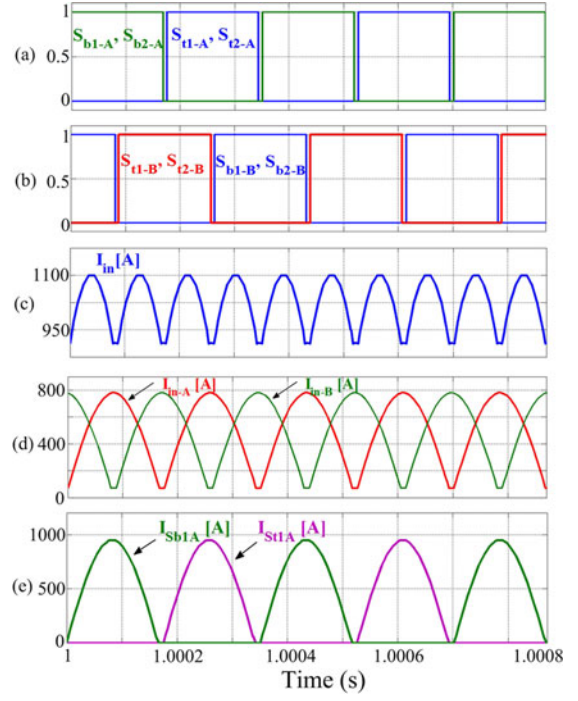


Fig. 12. Current waveforms of the 14-level RSC converter. (a) and (b) Switching patterns. (c) Input current. (d) Input currents of cells A and B. (e) Switch currents of cell A.

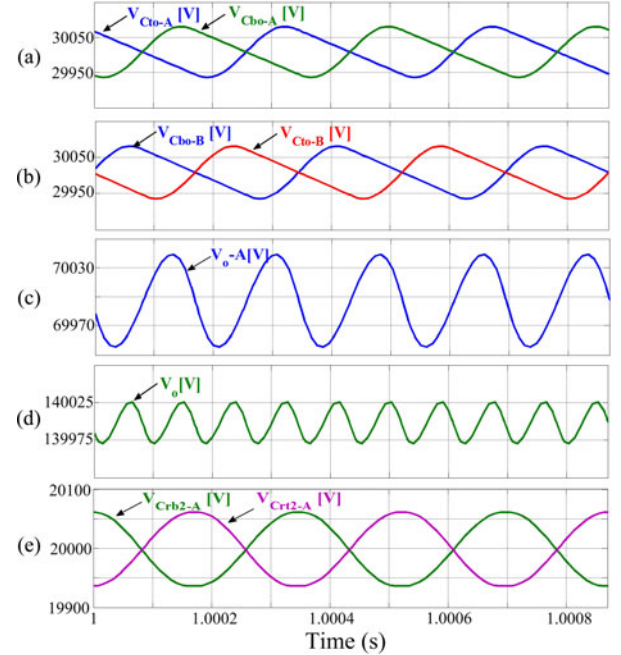


Fig. 13. Voltage waveforms of the 14-level RSC converter. (a) and (b) Output filter capacitor voltages. (c) Output voltage of cell A. (d) Output voltage. (e) Resonant capacitor voltages of cell A.

lation results in Fig. 13(d), the output voltage reaches 140 kV dc. The output voltage ripple can be reduced to the less than 80 V because of the interleaving functionality between the cells A and B.

Here, the proposed RSC converter is evaluated against the ZCS-RSC converter in [20]. Two configurations are

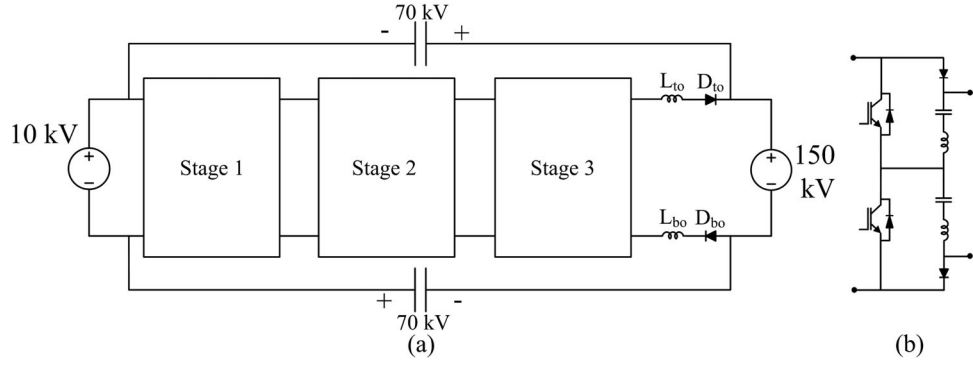


Fig. 14. (a) Proposed cascade RSC configuration. (b) Basic cell.

demonstrated to highlight the advantages of the proposed RSC converter as follows:

#### A. Series-Modular Configurations

The series-modular configurations are designed with the specifications such as input voltage, output voltage, and input power, used in simulation. Therefore, two modular cells A and B are designed for equal voltage gains of 7 as shown in Fig. 11(a). The voltage and current stresses of the components can be obtained based on Table I for the proposed RSC and ZCS-RSC converters.

#### B. Cascade Configurations

For the cascade configurations, an input of 10-kV dc will be boosted to the 150-kV dc for HVDC transmission. Therefore, three stages of the proposed RCS converter must provide a voltage gain of 15 ( $2^4 - 1$ ), as indicated in Fig. 14(a) and (b). The voltage and current ratings of the components for the proposed converter can be obtained from (8) to (14) and (44) in the Appendix. For the cascade ZCS-RSC configuration, seven stages are required to achieve a voltage gain of 15. Each stage consists of two resonant inductors, two resonant capacitors, two output filter capacitors, and four diodes [20].

For all the configurations, each switch or diode is comprised of several series and parallel-connected devices to withstand the rated current and voltage. The switching frequency, inductances, and resonant capacitor values are the same as those in the simulation for both RSC and ZCS-RSC converters. The output filter capacitors are considered larger than the resonant capacitors in the ZCS-RSC configurations as discussed in Section II-D. The suitable high-power capacitors and inductors with their weights and sizes are selected from AVX, GS-ESI, and REO [29]–[31]. These converters are compared based on the following features: 1) total number of devices; 2) passive component weights and volumes; and 3) losses.

#### C. Discussion

Fig. 15 shows the device count comparisons between series-modular and cascade configurations of the proposed RSC and ZCS-RSC converters. It can be seen that the cascade RSC converter requires a larger switch count compared to the series-

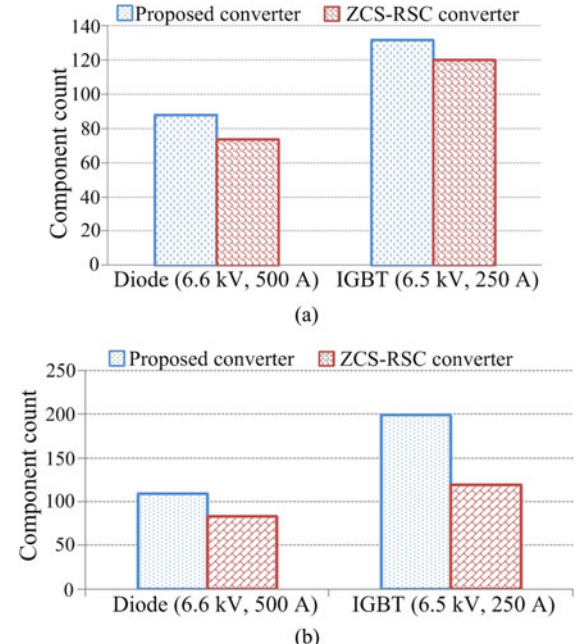


Fig. 15. Power device count comparisons. (a) Series-modular configurations. (b) Cascade configurations.

modular RSC converter due to the higher voltage and current ratings of the switches. For the ZCS-RSC converter, the voltage and current stresses of the diodes are the input voltage and output current that results in a decrease in the diode count and conduction losses.

In Figs. 16(a) and 17(a), the passive component losses are alleviated for the proposed series-modular and cascade configurations due to reduced number and lower current rating of the passive components. The normalized total loss values suggest that the proposed series-modular RSC converter yields approximately similar system losses to that of the ZCS-RSC converter. The proposed series-modular RSC converter achieves an efficiency of higher than 98%. On the other hand, the cascade RSC configuration has higher losses because an increase in the number of power devices in series will increase the switch and diode conduction losses.

It can be observed from Figs. 16(b) and 17(b) that the passive component volumes and weights are reduced significantly

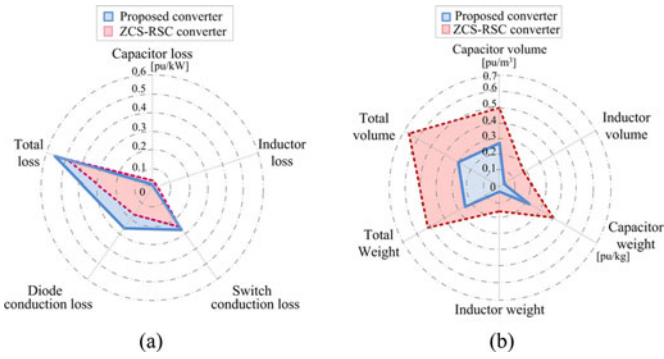


Fig. 16. Normalized comparisons between series-modular configurations. (a) Loss comparisons. (b) Weight and volume comparisons of the passive components.

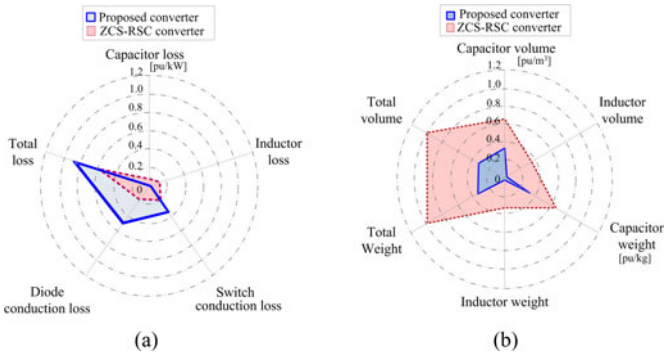


Fig. 17. Normalized comparisons between cascade configurations. (a) Loss comparisons. (b) Weight and volume comparisons of the passive components.

in the cases of the proposed series-modular and cascade RSC configurations. This is because the fact that the passive component counts in the ZCS-RSC converter are much larger than those of the proposed RSC configurations. For example, the cascade ZCS-RSC converter uses 14 inductors and 28 capacitors, whereas the proposed cascade RSC circuit requires eight inductors and eight capacitors (see Fig. 14) with lower current ratings in its circuit. The normalized TVAR requirements for the resonant capacitors are 24 and 56 in the cascade RSC and ZCS-RSC configurations, respectively (see Fig. 9). Although the RSC cascade configuration has two filter capacitors with the voltage stresses of  $7V_s$ , the ZCS-RSC converter requires 14 filter capacitors with the voltage ratings of  $V_s$ , larger capacitances, and higher current ratings. For example, a tripling of the capacitance requires an increase in the volume and weight of the capacitor by a factor of approximately 2 [30]. If the same low-voltage ripple is considered for all resonant capacitors, the ZCS-RSC converter requires larger resonant capacitances due to the higher current ratings of the capacitors. Therefore, the total weight of the capacitors in the ZCS-RSC configurations will be four times heavier than those of the proposed RSC configurations. Consequently, the normalized power density (pu/kg) of the proposed configurations can be enhanced more than two and three times those of the ZCS-RSC converter power density in these comparisons.

TABLE III  
SPECIFICATIONS OF THE CAPACITORS AND INDUCTORS

Components	Symbols	Value	Unit
Resonant inductor	$L_{rt1}, L_{rb1}$	14	$\mu\text{H}$
Resonant inductor	$L_{rt2}, L_{rb2}$	14	$\mu\text{H}$
Output inductor	$L_{to}, L_{bo}$	14	$\mu\text{H}$
Resonant capacitor	$C_{rt1}, C_{rb1}$	200	$\mu\text{F}$
Resonant capacitor	$C_{rt2}, C_{rb2}$	200	$\mu\text{F}$
Output capacitor	$C_{to}, C_{bo}$	200	$\mu\text{F}$

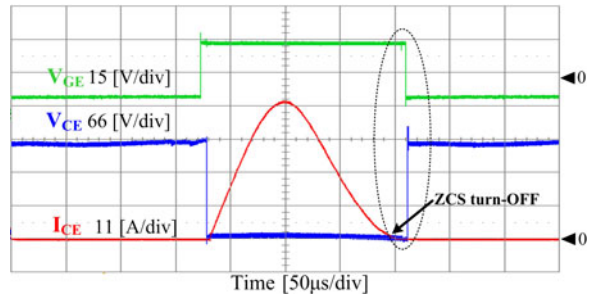


Fig. 18. Voltage and current waveforms of the switch  $S_{b2}$ .

The physical size of the power conversion systems is an important issue because they must be taken to the places where offshore wind turbines are located. Bulky and huge electrical components incur high investment costs due to the more difficult erection, large cranes, lifting vessels, and the equipment transportation from the shore to the installation sites. In other words, if the high-power-density electrical components are utilized in offshore wind farms, offshore floating platforms can be fully assembled and installed with a reduced burden for large vessels. Conceptual comparisons of the proposed configurations to the ZCS-RSC configurations show that the proposed converter is superior to the ZCS-RSC converter in terms of the passive component count, current, and total power ratings of the passive components, volume and weight. With the development of SiC technology in high-voltage applications, the devices with a higher switching speed, higher temperature operation, and greater voltage blocking capability will reduce the size of the passive components and increase the converter efficiency in the near future.

#### IV. EXPERIMENTAL RESULTS

The proposed seven-level RSC converter was implemented on a 5-kW laboratory prototype converter to verify the theoretical developments presented previously. The proposed converter was designed to boost a 100-V input to the maximum output voltage of 700 V. The switching frequency is about 2.8 kHz. Table III lists the specifications of the capacitors and inductors. Fig. 18 shows the voltage and current waveforms of the switch  $S_{b2}$ .  $V_{GE}$  is the gate-emitter voltage of  $S_{b2}$ ,  $V_{CE}$  is the collector-emitter voltage of  $S_{b2}$ , and  $I_{CE}$  is the collector-emitter current of  $S_{b2}$ . From Fig. 18, it can be seen that  $I_{CE}$  drops to

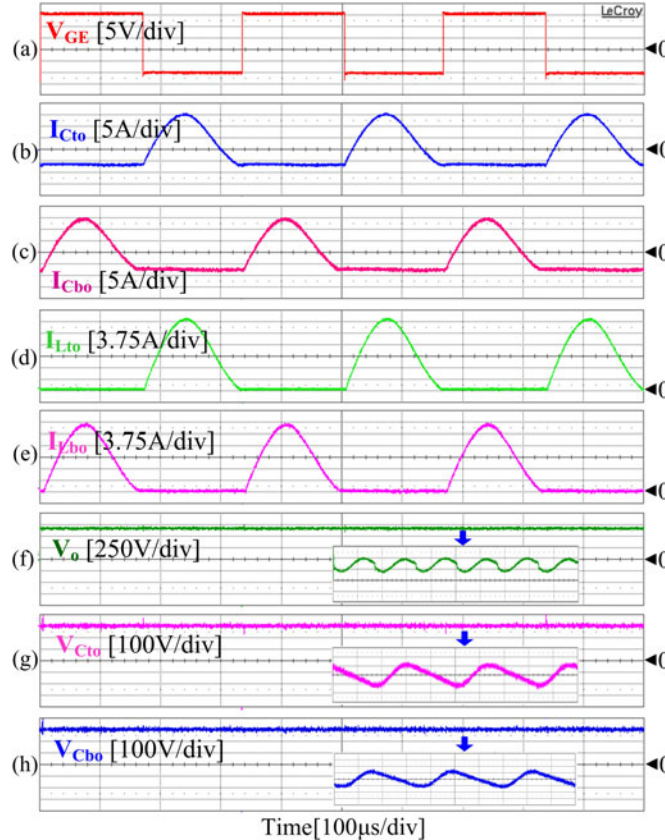


Fig. 19. Operating waveforms of the proposed converter. (a) Gate-emitter voltage of switch  $S_{b2}$ . (b) and (c) Output capacitor currents. (d) and (e) Output inductor currents. (f) Output voltage. (g) and (h) Output filter capacitor voltages.

zero before the switching transition to realize the zero-current. Consequently, all switches can be turned ON and OFF under the zero-current condition. Fig. 19(b), (c), (d), and (e) shows the experimental current waveforms of the output capacitors and output inductors.

It can be observed that the current waveforms closely match the analysis of (2) and (6) in Section II and the simulation results of Fig. 4(d) and (g). The peak value of the output inductor current is 22.5 A, which is consistent with the analysis of (2). The output voltage  $V_o$  and output filter capacitor voltages  $V_{Cto}$  and  $V_{Cbo}$ , are shown in Fig. 19(f), (g), and (h). These voltages have peak to peak voltage ripples of 4 and 10 V, respectively. The output voltage has a frequency twice that of the switching frequency due to the 180° phase shift between the top and bottom output filter capacitor voltages. The empirical voltages are in a close agreement with the analytical and simulation results in Figs. 8 and 13, respectively. The efficiency of the seven-level RSC converter for a different load was tested and the result is shown in Fig. 20. The efficiency reaches more than 95%, which is good considering that the converter is a prototype. The performance should be improved at higher power and voltage levels due to the lower switch conduction and passive component losses. The test results clearly show that the proposed circuit can enhance the power density and efficiency owing to the minimum switching losses.

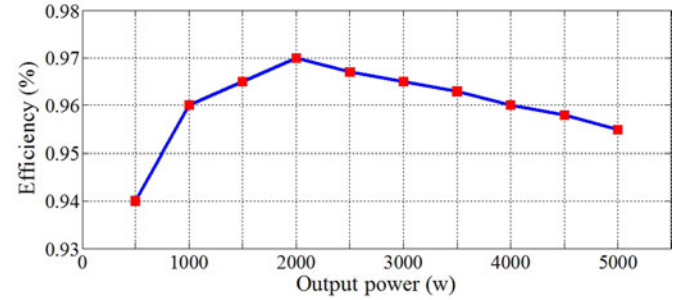


Fig. 20. Efficiency curve of the proposed seven-level RSC converter.

## V. CONCLUSION

A new RSC cell-based dc/dc converter with a high voltage gain is proposed for offshore wind energy applications. The soft-switching action is provided by the resonant condition of the circuit. Therefore, the switching losses are minimal in both ON and OFF instants, and the power density of the system can be enhanced by increasing the switching frequency. Output filter capacitor voltages are phase shifted by 180° with respect to each other to eliminate the output voltage ripples without adding extra components. The proposed series-modular and cascade RSC configurations have the inherent advantage of being readily applicable to multistage power switching converters. Conceptual comparisons of the proposed converter to a counterpart show that the proposed converter is well suited for high-voltage and high-power offshore wind applications requiring a high-power density and high efficiency. The simulation and experimental results confirm to verify the feasibility of the proposed converter.

## APPENDIX

Generalized equations are represented for the proposed  $k$ -stage RSC converter at the steady-state as follows:

From (2) and (3), the resonant capacitor current of the  $k$ th stage can be directly obtained as

$$i_{C_{rt(k)}}(t) = \frac{\pi P_o}{V_o} \sin(\omega_r t). \quad (31)$$

Since the top resonant capacitors and bottom resonant capacitors are charged and discharged by a 180° phase shift with respect to each other, the bottom resonant capacitor can be expressed as

$$i_{C_{rb(k)}}(t) = -\frac{\pi P_o}{V_o} \sin(\omega_r t). \quad (32)$$

In Mode III, all the top switches are ON, whereas all the bottom switches are OFF. Therefore, the top resonant capacitor currents in this mode ( $T_s/2 \leq t \leq T_s$ ) can be represented as

$$i_{C_{rt(k-1)}}(t) = i_{C_{rt(k)}}(t) - i_{C_{rb(k)}}(t) = -\frac{2\pi P_o}{V_o} \sin(\omega_r t) \quad (33)$$

$$i_{C_{rt(k-2)}}(t) = i_{C_{rt(k-1)}}(t) - i_{C_{rb(k-1)}}(t) = -\frac{4\pi P_o}{V_o} \sin(\omega_r t) \quad (34)$$

$$i_{C_{rt(k-3)}}(t) = i_{C_{rt(k-2)}}(t) - i_{C_{rb(k-2)}}(t) = -\frac{8\pi P_o}{V_o} \sin(\omega_r t) \quad (35)$$

$$i_{C_{rt(1)}}(t) = i_{C_{rt(2)}}(t) - i_{C_{rb(2)}}(t) = -\frac{2^{k-1}\pi P_o}{V_o} \sin(\omega_r t). \quad (36)$$

Similarly, the top and bottom resonant capacitor currents of the  $h$ th stage during one switching period can be obtained as

$$i_{C_{rh}}(t) = \frac{2^{k-h}\pi P_o}{V_o} \sin(\omega_r t), \quad (h = 1, 2, \dots, k) \quad (37)$$

$$i_{C_{rbh}}(t) = -\frac{2^{k-h}\pi P_o}{V_o} \sin(\omega_r t), \quad (h = 1, 2, \dots, k). \quad (38)$$

In Mode I and Mode III, the input current can be defined as

$$i_{in}(t) = \begin{cases} \sum_{i=1}^k i_{D_{ti}}(t) - i_{C_{to}}(t) & 0 \leq t \leq T_s/2 \\ i_{S_{t1}}(t) - i_{C_{to}}(t) & T_s/2 \leq t \leq T_s \end{cases}. \quad (39)$$

Substituting (6), (11), and (13) into (39) yields

$$i_{in}(t) = \frac{P_o}{V_o} + \left| (2^k - 1) \frac{\pi P_o}{V_o} \sin(\omega_r t) \right|. \quad (40)$$

From (40), the average input current can be calculated as

$$I_{in} = \frac{1}{T_s} \int_0^{T_s} i_{in}(t) dt = (2^{k+1} - 1) I_o. \quad (41)$$

From the aforementioned assumptions in Section II-B,

$$V_s I_{in} = V_o I_o. \quad (42)$$

Combining (41) and (42), the output voltage can be represented by

$$V_o = (2^{k+1} - 1) V_s. \quad (43)$$

From (43) and the proposed converter operation described in Section II, the resonant capacitor voltage of  $C_{rth}$  can be expressed as

$$V_{C_{rth}} = 2^{h-1} V_s, \quad (h = 1, 2, \dots, k). \quad (44)$$

Because the resonant capacitors in the top cell have the same power ratings with the counterparts in the bottom cell, the term  $TVAR_{C_r}$  can be defined as

$$TVar_{C_r} = 2 \sum_{h=1}^k V_{C_{rth}} I_{C_{rth}}. \quad (45)$$

Substituting (37) and (44) into (45) gives

$$\begin{aligned} TVar_{C_r} = & 2(V_s 2^{k-1} I_o + 2V_s 2^{k-2} I_o + 4V_s 2^{k-3} I_o \\ & + \dots + 2^{k-1} V_s I_o) = V_s I_o k 2^k \end{aligned} \quad (46)$$

## REFERENCES

- [1] J. M. Carrasco, L. G. Franquelo, J. T. Bialasiewicz, E. Galvan, R. P. Guisado, M. A. Prats, J. I. Leon, and N. M. Alfonso, "Power-electronic systems for the grid integration of renewable energy sources: a survey," *IEEE Trans. Ind. Electron.*, vol. 53, no. 4, pp. 1002–1016, Aug. 2006.
- [2] T. Kawaguchi, T. Sakazaki, T. Isobe, and R. Shimada, "Offshore wind farm configuration using diode rectifier with MERS in current link topology," *IEEE Trans. Ind. Electron.*, vol. 60, no. 7, pp. 2930–2937, Jul. 2013.
- [3] M. Liserre, R. Cardenas, M. Molinas, and J. Rodriguez, "Overview of multi-MW wind turbines and wind parks," *IEEE Trans. Ind. Electron.*, vol. 58, no. 4, pp. 1081–1096, Apr. 2011.
- [4] F. Blaabjerg and K. Ma, "Future on power electronics for wind turbine systems," *IEEE J. Emerg. Sel. Topics Power Electron.*, vol. 1, no. 3, pp. 139–152, Sep. 2013.
- [5] S. Gjerde, P. K. Olsen, K. Ljokelsoy, and T. Undeland, "Control and fault handling in a modular series connected converter for a transformerless 100 kV low weight offshore wind turbine," *IEEE Trans. Ind. Appl.*, vol. 50, no. 2, p. 1094–1105, Mar./Apr. 2013.
- [6] W. Musial and B. Ram. (2010, Sep.). Large-scale offshore wind power in the United States. Tech. Rep. National Renewable Energy Laboratory (NREL), USA/TP-500-40745. [Online]. Available: <http://www.nrel.gov/wind>
- [7] A. Garces and M. Molinas, "A study of efficiency in a reduced matrix converter for offshore wind farms," *IEEE Trans. Ind. Electron.*, vol. 59, no. 1, pp. 184–193, Jan. 2012.
- [8] A. Parastar and J. K. Seok, "High-power-density power conversion systems for HVDC-connected offshore wind farms," *J. Power Electron.*, vol. 13, no. 5, pp. 746–756, Sep. 2013.
- [9] C. Meyer, M. Hoing, A. Peterson, and R. W. De Doncker, "Control and design of DC grids for offshore wind farms," *IEEE Trans. Ind. Appl.*, vol. 43, no. 6, pp. 1475–1482, Nov./Dec. 2007.
- [10] T. Nguyen, D. Lee, and C. Kim, "A series-connected topology of diode rectifier and voltage-source converter for HVDC transmission system," *IEEE Trans. Power Electron.*, vol. 29, no. 4, pp. 1579–1584, Apr. 2014.
- [11] R. Li, S. Bozhko, and G. Asher, "Frequency control design for offshore wind farm grid with LCC-HVDC link connection," *IEEE Trans. Power Electron.*, vol. 23, no. 3, pp. 1085–1092, May 2008.
- [12] G. Ortiz, J. Biela, and J. W. Kolar, "Optimized design of medium frequency transformers with high isolation requirements," in *Proc. IEEE Ind. Electron. Soc.*, 2010, pp. 631–638.
- [13] G. Ortiz, J. Biela, and J. W. Kolar, "1 megawatt, 20 kHz, isolated, bidirectional 12 kV to 1.2 kV DC–DC converter for renewable energy applications," in *Proc. IEEE Int. Conf. Power Electron.*, 2010, pp. 3212–3219.
- [14] K. Hatua, S. Dutta, A. Tripathi, S. Baek, G. Karimi, and S. Bhattacharya, "Transformer less intelligent power substation design with 15 kV SiC IGBT for grid interconnection," in *Proc. IEEE Energy Conversion Congr. Expo.*, 2011, pp. 4225–4232.
- [15] S. P. Engel, N. Soltau, H. Stagge, and R. W. De Doncker, "Dynamic and balanced control of three-phase high-power dual-active bridge DC/DC converters in DC-grid applications," *IEEE Trans. Power Electron.*, vol. 28, no. 4, pp. 1880–1889, Dec. 2012.
- [16] N. Denniston, A. Massoud, S. Ahmed, and P. Enjeti, "Multiple-module high-gain high-voltage DC–DC transformers for offshore wind energy systems," *IEEE Trans. Power Electron.*, vol. 58, no. 5, pp. 1877–1886, May 2011.
- [17] N. Mohan, T. M. Undeland, and W. P. Robbin, *Power Electronics Converters, Application And Design*. New York: Wiley, 1995.
- [18] I. Laird and D. D. C. Lu, "High step-up DC/DC topology and MPPT algorithm for use with a thermoelectric generator," *IEEE Trans. Power Electron.*, vol. 28, no. 7, pp. 3147–3157, Jul. 2013.
- [19] K. K. Law, K. W. E. Cheng, and Y. P. B. Yeung, "Design and analysis of switched-capacitor-based step-up resonant converters," *IEEE Trans. Circuits Syst. I, Reg. Papers*, vol. 52, no. 5, pp. 943–948, May 2005.
- [20] W. Chen, A. Q. Huang, C. Li, G. Wang, and W. Gu, "Analysis and comparison of medium voltage high power DC/DC converters for offshore wind energy systems," *IEEE Trans. Power Electron.*, vol. 28, no. 4, pp. 2014–2023, Apr. 2013.
- [21] W. Qian, H. Cha, F. Z. Peng, and L. M. Tolbert, "55 kW variable 3X DC–DC converter for plug-in hybrid electric vehicles," *IEEE Trans. Power Electron.*, vol. 27, no. 4, pp. 1668–1678, Apr. 2012.
- [22] K. Zou, M. J. Scott, and J. Wang, "A switched-capacitor voltage tripler with automatic interleaving capability," *IEEE Trans. Power Electron.*, vol. 27, no. 6, pp. 2857–2868, Jun. 2012.
- [23] D. Cao and F. Z. Peng, "Zero-current-switching multilevel modular switched-capacitor DC–DC converter," *IEEE Trans. Ind. Appl.*, vol. 46, no. 6, pp. 2536–2544, Nov./Dec. 2010.
- [24] F. H. Khan and L. M. Tolbert, "A multilevel modular capacitor-clamped DC–DC converter," *IEEE Trans. Ind. Appl.*, vol. 43, no. 6, pp. 1628–1638, Nov./Dec. 2007.

- [25] F. Zhang, F. Z. Peng, and Z. Qian, "Study of the multilevel converters in DC–DC applications," in *Proc. IEEE Power Electron. Spec. Conf.*, 2004, pp. 1702–1706.
- [26] D. Gravoc and M. Purschel. (2009, Jan.). IGBT power losses calculation using the data-sheet parameters. Appl. note, vol. 1.1. [Online]. Available: <http://www.infineon.com>
- [27] Z. Liang, A. Q. Huang, and R. Guo, "High efficiency switched capacitor buck-boost converter for PV application," in *Proc. IEEE Appl. Power Electron. Conf. Expo.*, 2010, pp. 1951–1958.
- [28] (2013, Nov.). [Online]. Available: <http://www.plexim.com>
- [29] (2013, Nov.). [Online]. Available: <http://www.ga.com>
- [30] (2013, Nov.). [Online]. Available: <http://www.avx.com>
- [31] (2013, Nov.). [Online]. Available: <http://www.reo.de>



**Amir Parastar** (S'11) received the B.S. and M.S. degrees from the Department of Electrical Engineering, Islamic Azad University, Science and Research branch, Tehran, Iran, in 2004 and 2008, respectively. He is currently working toward the Ph.D. degree in the Power Conversion Laboratory, Department of Electrical Engineering, Yeungnam University, Gyeongsan, Korea.

His current research interests include high-power dc/dc conversion systems and power converter control of offshore wind farms.



**Jul-Ki Seok** (S'94–M'98–SM'09) received the B.S., M.S., and Ph.D. degrees from Seoul National University, Seoul, Korea, in 1992, 1994, and 1998, respectively, all in electrical engineering.

From 1998 to 2001, he was a Senior Engineer with the Production Engineering Center, Samsung Electronics, Suwon, Korea. Since 2001, he has been a Member of the faculty of the School of Electrical Engineering, Yeungnam University, Gyeongsan, Korea, where he is currently a Professor. His research interests include motor drives, power converter control of offshore wind farms, and nonlinear system identification related to the power electronics field.

Dr. Seok serves as an Associate Editor of the IEEE TRANSACTIONS ON INDUSTRY APPLICATIONS.